CONFERENCE PRE-PRINT

EXPERIMENTAL ANALYSES AND NUMERICAL MODELLING OF TRACE NEON SHATTERED PELLET INJECTION DISCHARGES ON JET

[1]M. KONG, [2]S. JACHMICH, [3]E. NARDON, [1]U. SHEIKH, [2]F.J. ARTOLA, [4]D. BONFIGLIO, [5]M. HOELZL, [6]D. HU, [5]A. PATEL, [5]W. TANG, [7]A. BOBOC, [8]G. BODNER, [7]Z. HUANG, [9]A. MATSUYAMA, [5]G. PAPP, [10]R. SAMULYAK, [7]S. SILBURN, [a]the JOREK Team, [b]JET Contributors and [c]the EUROfusion Tokamak Exploitation Team

[1]École Polytechnique Fédérale de Lausanne (EPFL), Swiss Plasma Center (SPC), Lausanne, Switzerland
[2]ITER Organization, Saint Paul-lez-Durance
[3]CEA, IRFM, Saint-Paul-lez-Durance, France
[4]Consorzio RFX and CNR-ISTP, Padova, Italy
[5]Max Planck Institute for Plasma Physics, Garching b. M., Germany
[6]School of Physics, Beihang University, Beijing, China
[7]UKAEA, Abingdon, United Kingdom of Great Britain and Northern Ireland
[8]General Atomics, San Diego, United States of America
[9]Graduate School of Energy Science, Kyoto University, Uji, Japan
[10]Stony Brook University, Stony Brook, United States of America

Email: mengdi.kong@epfl.ch

Abstract

A series of trace neon shattered pellet injection (SPI) discharges carried out in the final JET campaigns are investigated via experimental analyses as well as numerical modelling with the 3D non-linear MHD code JOREK and the 1.5D transport code INDEX. Experimentally, the cooling time defined as the time delay between the arrival of the first fragments at the plasma edge and the spike of the plasma current, drops from about 70ms with deuterium (D2) SPI to about 7ms with 0.016% neon SPI. INDEX and JOREK simulations suggest that plasmoid drifts are weaker in the 0.016% neon SPI case than in the D2 SPI case and that there is no evident drift with 0.5% neon SPI. On the other hand, 3D JOREK simulations show that it is difficult to directly reproduce the short cooling time in these trace neon SPI discharges. This is hypothesized to result from the insufficient local cooling with a (toroidally) oversized plasmoid that is typically used in 3D MHD modelling due to the constraints in computational resources. Future work will focus on applying artificially condensed radiation sinks in 3D JOREK simulations to investigate the susceptibility of the plasma to local cooling and the necessary conditions to trigger the early thermal quench observed in these trace neon SPI experiments.

1. INTRODUCTION

Shattered pellet injection (SPI) is the current strategy for the disruption mitigation system (DMS) in future large tokamaks including ITER to mitigate three critical consequences arising from disruptive events: excessive heat loads, intense electromagnetic forces and the generation of runaway electrons (REs) [1]. Deuterium (D2) SPI, originally envisaged to contribute to RE avoidance in ITER via a strong dilution cooling before the thermal quench (TQ) [2], was shown to suffer from the $\boldsymbol{E} \times \boldsymbol{B}$ drift of the ablation plasmoid toward the tokamak low field side (LFS) based on simulations with the 3D non-linear MHD code JOREK [3], where $\boldsymbol{E}$ and $\boldsymbol{B}$ refer to the electric and magnetic field, respectively. The $\boldsymbol{E} \times \boldsymbol{B}$ drift originates from the vertical polarization induced inside the plasmoid by the ∇B drift [4] and has been studied further via 3D JOREK modelling, exhibiting a quantitative agreement with existing theory [5]. This drift could substantially limit the core density rise and restrain the effectiveness of the LFS D2 SPI strategy for RE avoidance. Trace neon SPI, where a small percentage of neon is added to hydrogen-isotope SPI, on the other hand, is envisaged in view of reducing the pressure imbalance of the plasmoid via stronger local radiation, thus suppressing plasmoid drifts and facilitating RE avoidance [6].

In this context, a good series of trace neon SPI discharges were obtained in the final campaigns on JET to explore the feasibility of the trace neon SPI scheme in substituting pure D2 SPI as a solution for RE avoidance, which is crucial for developing injection schemes for the ITER DMS. In this paper, we will present analyses of this series

[a] See the author list of M. Hoelzl et al 2024 Nucl. Fusion 64 112016
[b] See the author list of C.F. Maggi et al 2024 Nucl. Fusion 64 112012
[c] See the author list of E. Joffrin et al 2024 Nucl. Fusion 64 112019

of JET discharges based on available diagnostics as well as numerical modelling with JOREK [7] and the 1.5D transport code INDEX [8].

2. JET TRACE NEON SPI EXPERIMENTS

The series of JET discharges considered are H-mode plasmas with a nominal plasma current of 2.5 MA, on-axis toroidal magnetic field of 2.5 T and total stored energy of 4 MJ before SPI. A cylindrical pellet with a diameter of 10 mm and a nominal velocity of 350 m/s was shattered and injected into the plasma, with a neon atomic mixture ratio of 0.016%, 0.04%, 0.33%, 0.5%, 1% and 2%, respectively. This corresponds to, for example, about 1.26×10^{19} neon atoms in the 0.016% neon SPI case and 4×10^{20} in the 0.5% neon SPI case. Discharges with pure D2 SPI but otherwise the same setup were also performed to provide a clean reference. Repetitions of discharges were carried out to ensure at least one electron density and temperature profile measurement during the ablation of the SPI fragments in each case, given the relatively low temporal resolution of the Thomson scattering (TS) system (50 ms). Fast visible cameras were used to facilitate the detection of possible outward motion of SPI fragments due to the "rocket effect" originating from the drifts of the ablation plasmoids [9].

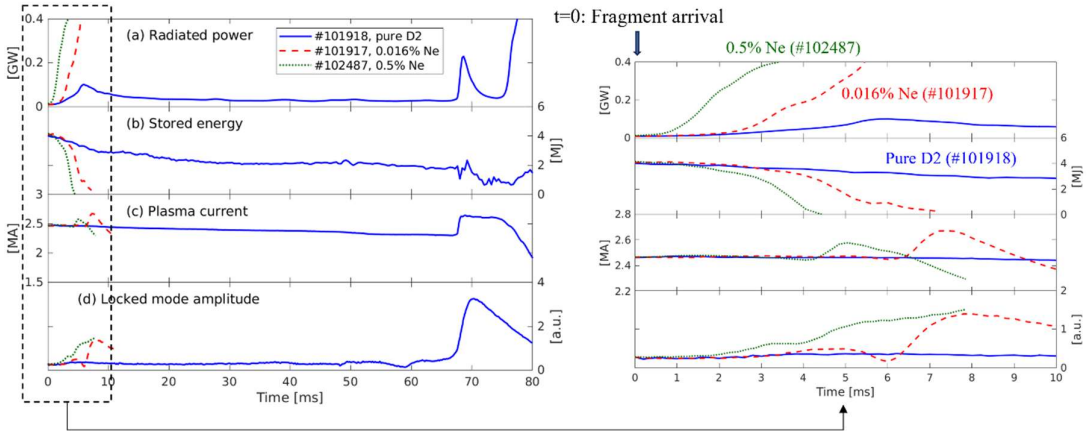

Fig. 1 Time-evolution of the (a) radiated power from the bolometer, (b) plasma stored energy from diamagnetic loops, (c) plasma current and (d) n=1 locked mode amplitude of JET SPI discharges with different neon concentrations: pure D2 in #101918 (solid blue), 0.016% neon in #101917 (dashed red) and 0.5% neon in #102487 (dotted green).

One key observation in this series of SPI discharges is that evident outward movement of the solid fragments, i.e., the rocket motion, was only observed in D2 SPI discharges, but not in trace neon SPI cases even with a neon atomic mixture ratio as low as 0.016% (at least up to the onset of the TQ) [10]. This indicates possible suppression of plasmoid drifts in trace neon SPI. Indeed, dedicated JOREK simulations demonstrated weaker drift with 0.016% neon SPI than with D2 SPI [10]. Another key observation, as illustrated in Fig. 1 (c), is that the cooling time already drops from about 70ms in the pure D2 SPI case (#101918, solid blue) to about 7ms with 0.016% neon (#101917, dashed red), where the cooling time refers to the duration between the arrival of SPI fragments at the plasma edge (denoted as $t = 0$) and the peak of the plasma current spike (as a result of a global reconnection event). Cases with higher neon concentrations exhibit similar cooling time as the 0.016% neon SPI case, for example, the 0.5% neon SPI discharge (#102487) has a cooling time of about 5ms. These have important implications for the effectiveness of the trace neon SPI scheme in RE avoidance: while the suppression of plasmoid drifts in trace neon SPI could improve the efficiency of core density rise, the accompanying shorter cooling time may affect the total material assimilated before the TQ onset.

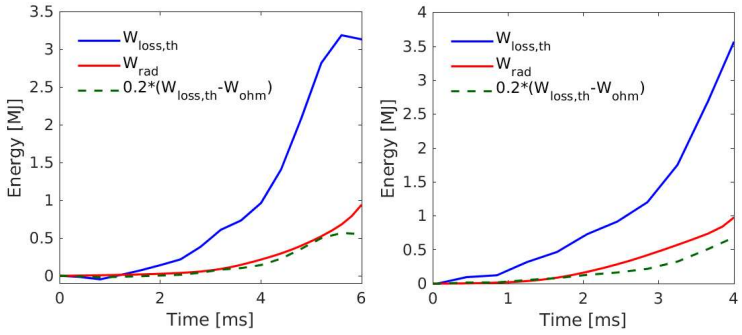

Fig. 2. Energy evolution of #101917 (left) and #102487 (right): thermal energy loss (blue), radiated energy (red), and 20% of the thermal energy loss excluding Ohmic heating since t=0 (dashed green) to guide the eyes.

To infer the main cooling mechanisms at play in these discharges, the time-evolution of the thermal energy loss and the radiated energy since $t = 0$ in #101917 and #102487 is depicted in Fig.2. We can see that the radiated fraction is below 30%, indicating that radiation does not play a key role in the thermal energy loss in these discharges (even when considering possible underestimation of the radiated power reconstructed from bolometer measurements [11]). It is thus expected that heat transport (for example due to strong MHD activities) plays a more important role. In this paper, we will present 3D JOREK simulations of #101917 and #102487 with a focus on their relatively short cooling time, as shown in section 3. In addition, initial INDEX simulations of these discharges with a focus on the plasmoid drift and material assimilation will be discussed in section 4.

3. 3D MHD MODELLING WITH THE JOREK CODE

3.1. JOREK model used and simulation setup

JOREK uses the finite element method in the poloidal plane and a Fourier decomposition in the toroidal direction to solve relevant equations. The JOREK model used in this paper comprises ansatz-based reduced MHD equations with parallel flows and an extension to impurities, solving the time-evolution of the poloidal magnetic flux, toroidal current density, poloidal flow potential, toroidal vorticity, plasma mass density, total plasma (ion and electron) pressure, parallel velocity and impurity mass density [7]. Two different treatments of the radiation from the injected impurities (via SPI) are applied and compared, one with the coronal equilibrium (CE) assumption for the charge state distribution and the other considering a collisional-radiative (CR) non-equilibrium impurity distribution [12]. In addition, uniform background impurities are considered assuming CE, with a tungsten level of $3 \times 10^{15} m^{-3}$ and neon density (left from previous discharges) of $1 \times 10^{17} m^{-3}$ in the simulations to match the total radiation level before the SPI. The same initial plasma equilibrium before SPI is used in all the JOREK simulations, considering very similar plasma scenarios in these discharges. The initial flux-surface-averaged electron density (n_e), electron temperature (T_e) and safety factor (q) profiles are shown in Fig. 2, where ψ_N is the normalized poloidal magnetic flux. We can see that the input n_e and T_e (assuming $T_i = T_e$) represent well the TS data. The Spitzer resistivity $\eta \propto T_e^{-3/2}$ is used for T_e up to 1.25keV, above which η is set to uniform for numerical reasons. The parallel heat diffusivity $\kappa_\parallel \propto T_e^{5/2}$ follows the Spitzer-Härm formulation. The perpendicular heat and particle diffusivities are set to $1\mathrm{m}^2\mathrm{s}^{-1}$, while the parallel particle transport is purely convective.

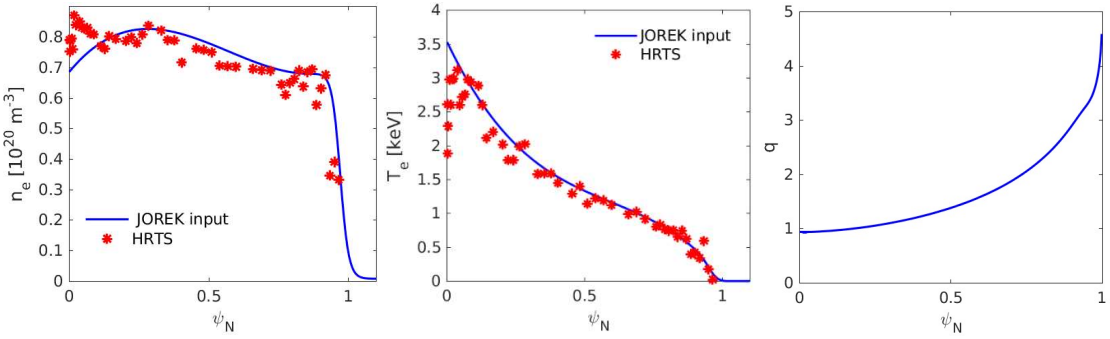

Fig. 2 JOREK input profiles (blue). The Thomson scattering data (red symbols) are taken from #102487 at 50.9255s.

The injected SPI fragments travel into the plasma following their injection trajectories, with a mass ablation rate $G \propto \lambda(X)\, T_e^{5/3} r_p^{4/3} n_e^{1/3}$ based on the neutral gas shielding (NGS) model [13,14], where r_p is the fragment radius, $\lambda(X) \equiv 27.08 + \tan(1.49X)$ and $X \equiv N_{D_2}/(N_{Ne} + N_{D_2})$ is the D2 molecular mixture ratio. T_e and n_e here are either taken from the local values at the position of the fragment ("local-ablation" model) or from the flux-surface-averaged values ("non-local ablation") to account for the long mean-free-path of the hot electrons seen by the fragment [15]. A "teleportation" model [3] is applied in simulations with plasmoid drifts, where the particle and energy transfers caused by drifts are considered by teleporting the ablation neutral source from the fragment location by a certain distance (ΔR) along the outward major radius direction, and by teleporting energy from the fragment location to the neutral location, at a rate corresponding to the ablation source times a few tens of eVs (ΔE). ΔE here considers the overall effects of dissociation, ionization, radiation and early heating before plasmoid drifts and is set to 50eV in these simulations. $\Delta R = 15$cm is used in all the simulations of #101917 shown in section 3.2.1, whereas no plasmoid drift is included in the simulations of #102487 in section 3.2.2, i.e. $\Delta R = 0$ and the ablated material is deposited locally around each fragment. In both cases the deposited material has a Gaussian shape in the radial, poloidal and toroidal direction, with a half e^{-1} width of $\Delta r = 4$ cm, $\Delta l_\theta = 8$ cm

and $\Delta\phi = 0.5$ rad, respectively, unless otherwise specified. Modes with toroidal mode number $n = 1,2, \ldots,10$ need to be included to resolve a simulation with $\Delta\phi = 0.5$ rad.

In terms of the SPI, the bulk velocities of the fragments are set to 170m/s and 185m/s in the 0.016% neon (#101917) and 0.5% neon SPI (#102487) cases, respectively, following the fast camera data and 2D JOREK scans [10]. A $\pm 40\%$ velocity spread around these bulk velocities is applied in both cases. The bulk velocities are only about half of the velocities estimated by the travel time and distance from a microwave cavity diagnostic (before pellet shattering) to the first light on the fast camera (fragments reaching the scrape-off layer). This is possibly due to shock waves generated in the shattered gas, which brake fragment penetration, similar to that in the massive gas injection [16]. In fact, the gas generated in the shattering process can take up to 20% of the initial pellet mass in the impact velocity range of interest based on laboratory measurements [17]. The size distribution of the fragments with respect to the distance between the fragment and the exit of the shattered tube (L_{RZ}) in the two discharges is shown in Fig. 3 (blue circles), following a fragmentation model [18] and the laboratory observation that the front and rear fragments are small [19]. Considering the loss of the pellet material due to the shattering process (in the form of shattered gas at the front of the SPI plume), we only retain (part of) the bulk and the rear fragments in the JOREK simulations, as depicted by the red crosses in Fig. 3.

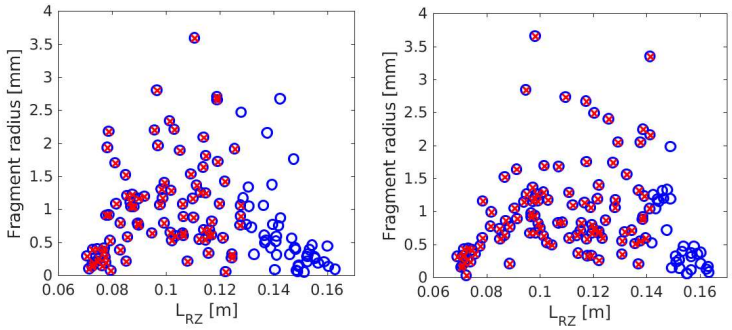

Fig. 3. Fragment radius distribution of #101917 (left) and #102487 (right). Blue circles: full distribution based on the fragmentation model; red crosses: selected fragments used in the JOREK modelling.

3.2. JOREK modelling results

3.2.1. Simulations of the 0.016% neon SPI discharge (#101917)

Three JOREK simulations of the 0.016% neon SPI discharge (#101917) are shown in Fig. 4, assuming CE for impurity radiation in all cases (simulations of this discharge with the CR model are on-going). The local-ablation model is used in the red case, while the non-local model is adopted in the other two cases, with $\Delta\phi = 0.5$ (green) and 0.2 (purple), respectively. Plasmoid drifts are considered in all the simulations here via the teleportation model and with a drift distance of 15cm, following the results in [10]. The synthetic central line-integrated density (n_{el}) from the JOREK simulations matches well that from the polarimeter. However, the total radiated power (P_{rad}) misses the sharp rise observed in the experiment at $t\sim$3ms, similarly for the plasma thermal energy that misses the fast drop in the experiment. Note that the thermal energy traces (solid lines) in Fig. 4 (right) are also scaled up (dotted lines) to compare better with the stored energy measured by the diamagnetic loops (solid blue), which includes contributions from fast particles that are not included in the simulations. The lower P_{rad} from $t\sim$2.5ms in the $\Delta\phi = 0.2$ case (purple) than the $\Delta\phi = 0.5$ case (green) originates from their slightly different n_e and T_e profile evolutions, as shown in Fig.5. The radiated power density profiles, as a result, are narrower in the $\Delta\phi = 0.2$ case and lead to a lower total radiated power shown in Fig. 4. The plasma thermal energy, however, drops slightly faster in the $\Delta\phi = 0.2$ case due to slightly stronger heat transport. As discussed in section 2 and shown in Fig. 2, the radiation loss does not dominate the thermal energy loss in this discharge, so the absence of the TQ in the JOREK simulations indicates that macroscopic MHD modes are not sufficiently strong in these simulations.

The MHD activities in the two simulations using the non-local ablation model (i.e., the green and purple cases) are illustrated by the Poincaré plots shown in Fig. 6. We can see that only weak MHD activities (mainly outside $q = 2$) exist and the core plasma remains largely unperturbed in both simulations. The absence of strong MHD modes suggests insufficient local radiative cooling at major rational surfaces (in particular $q = 2$). Once initialized, the strong local cooling could lead to sufficiently low T_e along the given flux tube (appearing as "T_e holes" in the plasma) that can increase the local plasma resistivity, alter strongly the local current density profile and trigger macroscopic current-driven modes. Indeed, as shown in Fig. 7, despite the stronger cooling and more evident T_e holes at $q = 3$, there is only weak and transient T_e holes at $q = 2$, which is not sufficient to trigger a large 2/1 mode. The lack of strong T_e holes at $q = 2$ in the simulations is hypothesized to result from the toroidally

oversized plasmoid applied in the simulations (due to constraints in computational resources) and the CE assumption used. Further JOREK simulations with artificially condensed radiation sinks are planned to investigate the susceptibility of the plasma to T_e holes and the necessary conditions to trigger the TQ observed in the experiment.

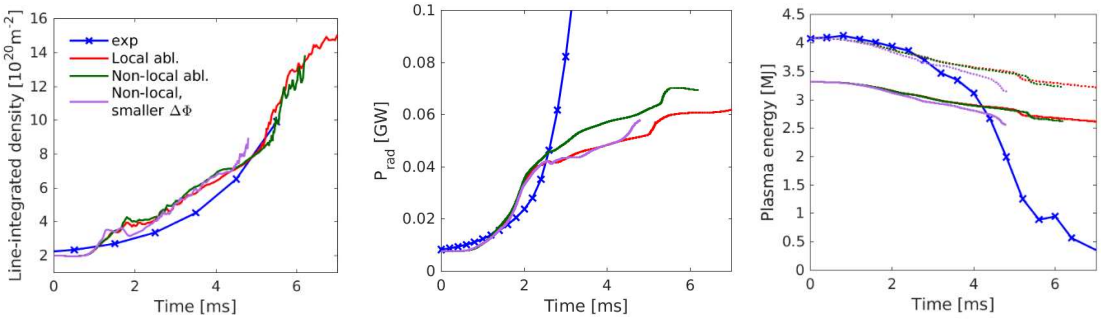

Fig. 4 Comparing JOREK simulations with experimental measurements: the central line-integrated density measured by the polarimeter(left), radiated power from the bolometer (middle) and plasma energy from the diamagnetic loops (right).

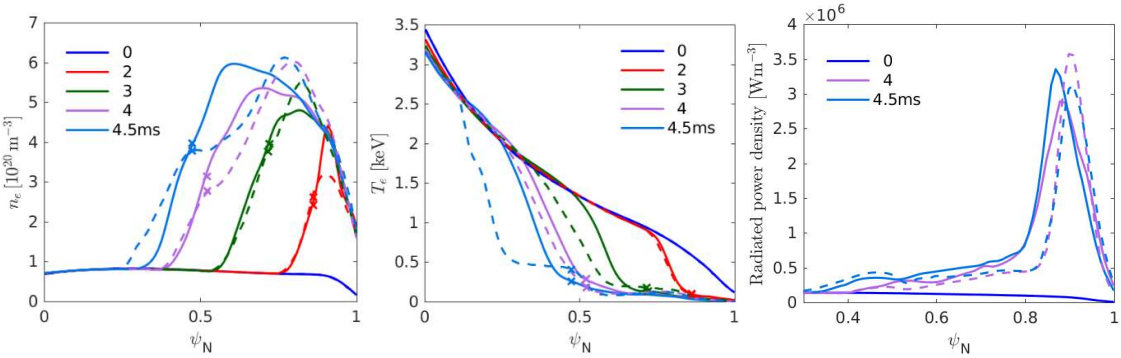

Fig. 5 n_e, T_e and radiated power density profiles at different time slices (as indicated by the legends) of the JOREK simulations with $\Delta\phi = 0.5$ (solid traces) and 0.2 (dashed), i.e., corresponding to the green and purple cases in Fig. 4, respectively. The location of the fragment that has the highest ablation rate at each time slice is marked by a cross with the corresponding color.

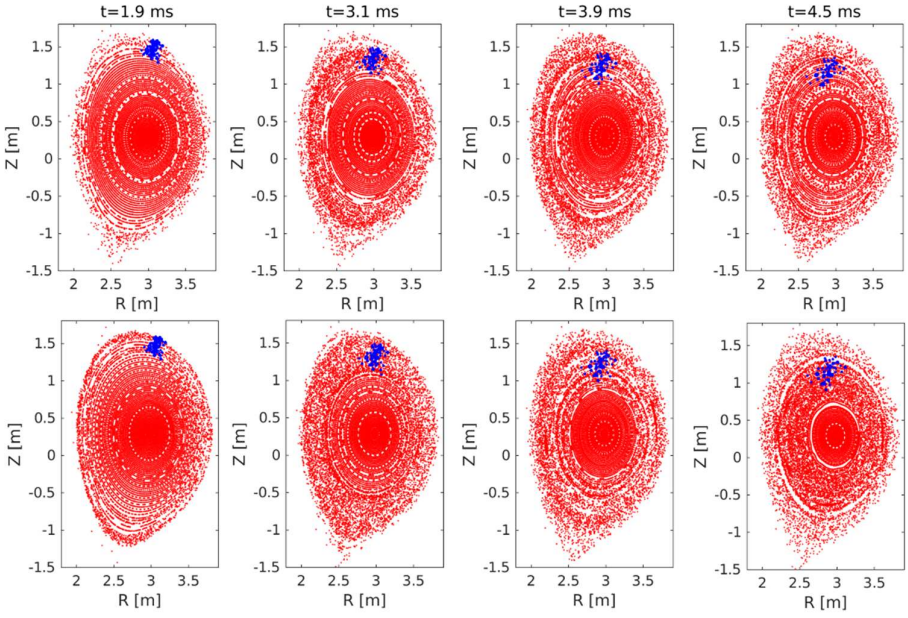

Fig. 6 Poincaré plots at different time slices of the simulations with $\Delta\phi$ =0.5 (top) and 0.2 (bottom), i.e., the green and purple cases shown in Fig. 4, respectively. The locations of the remaining fragments at each time slice are indicated by the blue symbols.

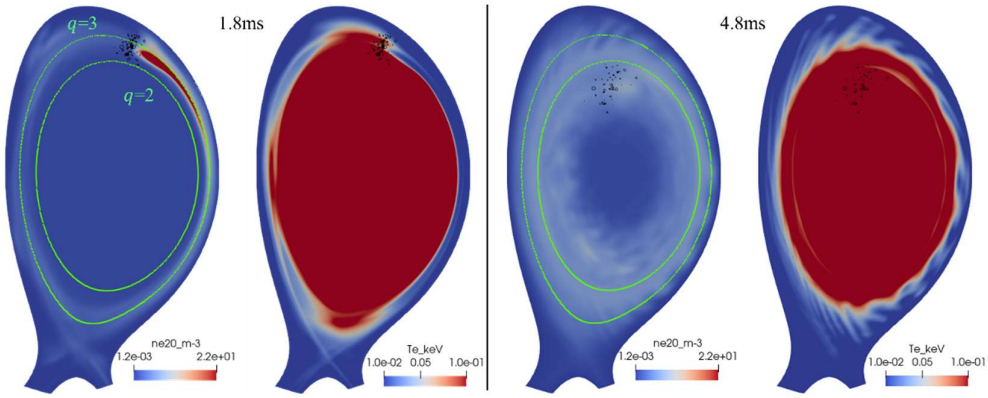

Fig. 7 n_e and T_e on the SPI injection plane at 1.8ms (left) and 4.8ms (right) of the simulation with $\Delta\phi$ =0.2. The remaining fragments are indicated by the black circles, while the ablated material is teleported outward to consider plasmoid drifts.

3.2.2. Simulations of the 0.5% neon SPI discharge (#102487)

Three different JOREK simulations of #102487 are considered here: one 2D simulation with the CE assumption of impurity charge distribution, one 2D simulation with the CR impurity model and one 3D simulation (including up to $n = 10$ toroidal harmonics) with the CR model. The time-evolution of n_{el} and P_{rad} are shown in Fig. 8 (left and middle plots), together with corresponding experimental measurements. The simulations have similar n_{el}, while the cases using the CR impurity model exhibit higher P_{rad}, as expected [12,13]. The 3D simulation with the CR model, however, still misses the rapid rise of P_{rad} from $t\sim$1ms and the fast drop of thermal energy (not shown here for conciseness), similar to that in the modelling of #101917. As discussed in the previous section, this is probably due to the mild macroscopic MHD activities ($n \leq 3$) in the simulation, as illustrated in Fig. 8 (right), which may result from the lack of strong local cooling (at $q = 2$). JOREK simulations with artificially condensed radiation sinks are planned to investigate their effect and the conditions of TQ onset in the experiment, similar to #101917 discussed in the previous section.

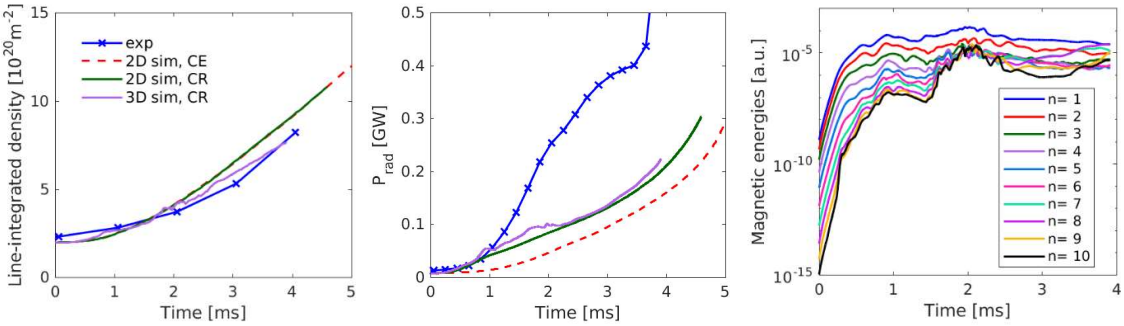

Fig. 8 (Left and middle) Comparing JOREK simulations with the central line-integrated density measured by the polarimeter and radiated power from the bolometer; (right) magnetic energy evolution of different toroidal harmonics in the 3D simulation with the CR model, i.e., the purple case in the left and middle plots.

4. MODELLING WITH THE INDEX CODE

Regarding the plasmoid drift and material assimilation, simulations with the 1.5D INDEX code were carried out to further interpret the experimental observations and establish reduced models. INDEX self-consistently solves 1D transport equations in flux coordinates coupled with a 2D Grad-Shafranov equilibrium solver. It has an SPI module that evaluates the ablation rate based on the NGS model. The fragment trajectories are evolved in 3D physical space and mapped onto the flux coordinates assuming toroidal symmetry of the plasma equilibrium. INDEX has been previously benchmarked with 2D JOREK simulations of the ITER plasma [8]. A back-averaging model is available in INDEX to model plasmoid drifts, where the ablated material from each fragment is distributed uniformly behind the fragment location. This model has been used to assess the impact of plasmoid drifts in previous AUG, JET and DIII-D SPI experiments [20-22].

In the simulations of the JET trace neon SPI discharges discussed here, INDEX uses the same target plasma and SPI setup as in JOREK, i.e., as those presented in section 3.1. In the simulations shown in Figs. 9, different back-averaging parameters are needed for different discharges to fit their respective TS measurements: 50% and 20% of the ablated material is shifted outward and deposited uniformly between the fragment location and $\psi_N = 1$ for the pure D2 SPI and 0.016% neon SPI discharges, respectively, while the remaining ablated material is deposited locally at the ablation location; in the 0.5% neon SPI case, however, all the ablated material is deposited locally and no material is shifted outward. This indicates that plasmoid drifts are reduced with 0.016% neon SPI (compared to D2 SPI) and that there is no evident drift with 0.5% neon SPI, similar to conclusions from previous JOREK simulations [10]. Further INDEX simulations will be performed to investigate the uncertainties and effects of the back-averaging parameters. The outward rocket motion of the solid fragments observed in D2 SPI experiments and considered in JOREK simulations [10] is included in the INDEX simulation of #101918 shown in Fig. 9. As seen from the comparison with the TS measurements (shown as symbols), this helps to recover the trend of the core fuelling in the later phase of the discharge (~12.4ms) since the remaining fragments that have reached the HFS of the plasma move radially outward and eventually fuel the plasma core. A more quantitative comparison with the experimental measurements and JOREK simulations are left for future work.

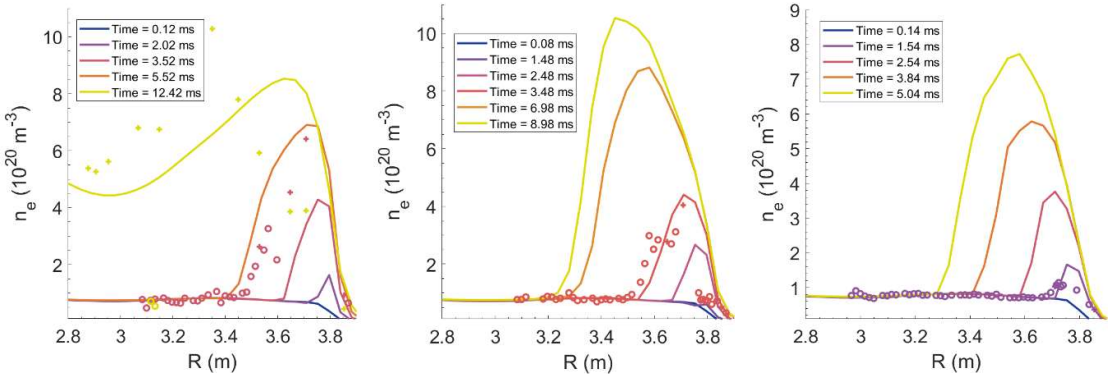

Fig. 9 n_e profile evolution at different time slices of the INDEX simulation of (left) #101918 (D2 SPI), (middle) #101917 (0.016% neon SPI) and (right) #102487 (0.5% neon SPI). TS measurements at approximately the same time slices are shown by the symbols with the same color: 3.52ms and 12.42ms for #101918, 3.48ms for #101917 and 1.54ms for #102487.

5. CONCULSIONS AND OUTLOOK

A series of trace neon SPI discharges were carried out in the final JET campaigns and were investigated via combining experimental measurements, 3D JOREK modelling and 1.5D INDEX simulations. Two key observations were made in these discharges: 1) evident outward movement of the fragments was observed in D2 SPI discharges, but not in trace neon SPI cases even with a neon mixture ratio as low as 0.016%; 2) the cooling time drops from about 70ms with D2 SPI to about 7ms already with 0.016% neon, while further increase in the neon concentration in the SPI does not change much the cooling time. INDEX simulations suggested that plasmoid drift is weaker in the 0.016% neon SPI case than in the D2 SPI case and that there is no evident drift with 0.5% neon SPI, similar to previous JOREK modelling results. Regarding the short cooling time, 3D JOREK simulations of the 0.016% and 0.5% neon SPI cases showed that it is difficult to directly recover the early TQ onset observed in the experiments. This is hypothesized to result from the insufficient local cooling with a (toroidally) oversized plasmoid that is typically used in 3D non-linear MHD modelling due to the constraints in computational resources. To circumvent this limitation, future work will focus on applying artificially condensed radiation sinks to investigate the susceptibility of the plasma to T_e holes and the necessary conditions to trigger the TQ observed in the experiments. Further INDEX simulations will also be performed, aiming at a quantitative comparison with the experiments and JOREK simulations.

ACKNOWLEDGEMENTS

This work has been carried out within the framework of the EUROfusion Consortium, funded by the European Union via the Euratom Research and Training Programme (Grant Agreement No 101052200 - EUROfusion). The Swiss contribution to this work has been funded by the Swiss State Secretariat for Education, Research and Innovation (SERI). Views and opinions expressed are however those of the author(s) only and do not necessarily reflect those of the European Union, the European Commission, SERI or the ITER Organization. Neither the

European Union nor the European Commission nor SERI nor the ITER Organization can be held responsible for them. This work was supported in part by the Swiss National Science Foundation.

REFERENCES

[1] JACHMICH, S. et al, Shattered pellet injection experiments at JET in support of the ITER disruption mitigation system design, Nucl. Fusion 62 (2022) 026012.

[2] NARDON, E. et al, Fast plasma dilution in ITER with pure deuterium shattered pellet injection, Nucl. Fusion 60 (2020) 126040.

[3] KONG, M. et al, Interpretative 3D MHD modelling of deuterium SPI into a JET H-mode plasma, Nucl. Fusion 64 (2024) 066004.

[4] PARKS, P.B., SESSIONS, W.D. and BAYLOR, L.R., Radial displacement of pellet ablation material in tokamaks due to the grad-B effect, Phys. Plasmas 7 (2000) 1968–75.

[5] KONG, M. et al, 3D MHD modelling of plasmoid drift following massive material injection in a tokamak, Nucl. Fusion 65 (2025) 016042.

[6] MATSUYAMA, A., Neutral gas and plasma shielding (NGPS) model and cross-field motion of ablated material for hydrogen–neon mixed pellet injection, Phys. Plasmas 29 (2022) 042501.

[7] HOELZL, M. et al, The JOREK non-linear extended MHD code and applications to large-scale instabilities and their control in magnetically confined fusion plasmas, Nucl. Fusion 61 (2021) 065001.

[8] MATSUYAMA, A. et al, Transport simulations of pre-thermal quench shattered pellet injection in ITER: code verification and assessment of key trends, Plasma Phys. Control. Fusion 64 (2022) 105018.

[9] MULLER, H.W. et al, High β plasmoid formation, drift and striations during pellet ablation in ASDEX Upgrade, Nucl. Fusion 42 (2002) 301–9.

[10] KONG, M., "Role of plasmoid drift in the efficiency and reliability of shattered pellet injection", O-079, paper presented at the 51st European Physical Society Conference on Plasma Physics, Vilnius, 2025; to be submitted to Plasma Phys. Control. Fusion.

[11] STEIN-LUBRANO, B. et al, Thermal energy mitigation and toroidal peaking effects in JET disruptions, Phys. Plasmas 32 (2025) 042510.

[12] HU, D. et al, Collisional-radiative non-equilibrium impurity treatment for JOREK simulations, Plasma Phys. Control. Fusion 63 (2021) 125003.

[13] HU, D. et al, Radiation asymmetry and MHD destabilization during the thermal quench after impurity shattered pellet injection, Nucl. Fusion 61 (2021) 026015.

[14] BOSVIEL, N., "Numerical studies of neon pellet ablation in tokamaks", P1.1102, paper presented at the 46th European Physical Society Conference on Plasma Physics, Milan, 2019.

[15] PEGOURIE, B., Modelling of pellet ablation in additionally heated plasmas, Plasma Phys. Control. Fusion 47 (2005) 17.

[16] NARDON, E. et al, On the mechanisms governing gas penetration into a tokamak plasma during a massive gas injection, Nucl. Fusion 57 (2017) 016027.

[17] GEBHART, T. E., BAYLOR, L. R., MEITNER, S. J., Shatter Thresholds and Fragment Size Distributions of Deuterium–Neon Mixture Cryogenic Pellets for Tokamak Thermal Mitigation. Fusion Sci. and Techno. 76 7 (2020) 831–835.

[18] GEBHART, T. E., BAYLOR, L. R., MEITNER, S. J., Experimental Pellet Shatter Thresholds and Analysis of Shatter Tube Ejecta for Disruption Mitigation Cryogenic Pellets, IEEE Trans. Plasma Sci. 48 (2020) 1598–605.

[19] GEBHART, T. E., BAYLOR, L. R., MEITNER, S. J., Analysis of the Shattered Pellet Injection Fragment Plumes Generated by Machine Specific Shatter Tube Designs. Fusion Sci. Technol. 77 1 (2021) 33–41.

[20] PATEL, A. et al, Modelling of shattered pellet injection experiments on the ASDEX Upgrade tokamak, Nucl. Fusion 65 (2025) 086031.

[21] SHEIKH, U., "Thermal Quench Dynamics of Shattered Pellet Injections on JET", UO06.00008, paper presented at the 66th Annual Meeting of the APS Division of Plasma Physics, Atlanta, Georgia, 2024.

[22] LVOVSKIY, A. et al, Density and temperature profiles after low-Z and high-Z shattered pellet injections on DIII-D, Nucl. Fusion 64 (2024) 016002.